Check for updates

Tunable uniaxial, area, and volume negative thermal expansion in quartz-like and diamond-like metal–organic frameworks

Lei Wang, ID *[a] Ying Chen,[b] Hideo Miura,[b] Ken Suzuki[b] and Cong Wang ID *[c]

This paper proposes that it will be an effective way to discover and explore organic negative thermal expansion (NTE) materials based on the specific topologies in inorganic NTE materials. Various NTE behaviors from the uniaxial, area, and volume-NTE can be achieved by adjusting the topology, for instance, quartz-like and diamond-like. $Zn(ISN)_2$ and $InH(BDC)$ metal–organic frameworks (MOFs) with quartz-like topology have been studied by first principles calculations. The calculated area-NTE of $Zn(ISN)_2$ and uniaxial-NTE of $InH(BDC)$ within quasi-harmonic approximation (QHA) agree well with the experimental data. Through the calculation of Grüneisen parameters, it is shown that low-frequency optical phonons appear dominant resulting in their NTE, but the coupling to high-frequency phonons is of greater ultimate importance. The lattice vibrational modes of great contribution to area-NTE of $Zn(ISN)_2$ and uniaxial-NTE of $InH(BDC)$ are analyzed in detail. Also, four MOFs with diamond-like topology are predicted to exhibit volume-NTE behavior. Moreover, it is found that there is a bulk modulus anomaly in some studied MOFs with the quartz-like and diamond-like framework, where the temperature dependence of bulk modulus does not follow the inverse dependence on that of volume. These specific topologies provide key geometric frameworks for various NTE behaviors of MOFs, and meanwhile, the local structure and bond environment in MOFs can lead to abnormal interatomic force, *i.e.*, bulk modulus anomaly. This abnormal elastic property also deserves more attention.

1. Introduction

Negative thermal expansion (NTE) materials that shrink upon heating are not only of particular interest but have important potential applications.[1] By using NTE materials to compensate for the more common positive thermal expansion (PTE) behavior of other materials, zero thermal expansion behavior in NTE/PTE composites can be achieved.[2–4] Crystal engineering has been concerned with the design of solids with specific, controlled properties. One such attractive property is NTE behavior. To satisfy more design requirements, all kinds of NTE from uniaxial, to area to volume are in demand. Several inorganic systems exhibiting adjustable NTE behavior are known but organic materials displaying tunable NTE behavior have rarely been reported.[5,6]

For inorganic materials, different NTE mechanisms may be involved.[7] Whereas, NTE behavior in organic materials often occurs for geometrical reasons, considering special geometrical arrangements of the atoms (molecules) and peculiarities of the bonding which restrict the thermal movement of the atoms (molecules).[8,9] Such NTE materials are characterized by open, underconstrained lattices or by a network of rigid, underconstrained entities. Within the scope of inorganic materials, following the specific crystal structure, other NTE candidates can be derived from a certain NTE system. For example, the diamond-like, rutile-like, as well as zinc blende-like materials, can be traced to the NTE property.[10–13] Similarly, the specific topology that dominates NTE behavior in inorganic materials can be an inspiration for looking for NTE candidates in organic materials.[14,15]

Quartz is an archetypal material exhibiting NTE behavior and possesses a framework structure of stiff units, namely SiO_4 tetrahedra, linked through shared oxygen atoms as very flexible hinges. Both phases of low-symmetry α-quartz (low temperature) and high-symmetry β-quartz (high temperature) show the NTE property.[16,17] It has been reported that $Ag_3[Co(CN)_6]$ and $Zn[Au(CN)_2]_2$ frameworks with the topology of β-quartz exhibit the coexistence of large uniaxial-NTE and negative linear compressibility (NLC) properties.[18–23] The NTE behavior in some materials such as Cu_2O, Ag_2O, $ZnSiP_2$, and so on is attributed to the tetrahedral coordination of the crystal which has similarities with diamond-like topology.[10,13]

[a]Department of Physics, University of Science and Technology Beijing, Beijing 100083, China. E-mail: leiw_phy@ustb.edu.cn; congwang@buaa.edu.cn

[b]Fracture and Reliability Research Institute, Graduate School of Engineering, Tohoku University, Sendai 980-8579, Japan

[c]School of Integrated Circuit Science and Engineering, Beihang University, Beijing 100191, China

Recently, metal–organic frameworks (MOFs) as a new class of materials are receiving considerable attention due to their potential applications in some fields such as catalysis, gas separation, gas storage, and so on.[24] MOFs can be designed by using flexible or rigid as well as mixed organic linkers which bind to the metal atoms that could provide structural diversity with various properties. The preparation and properties of quartz-like and diamond-like MOFs have been reported.[14,25–30] By the way, most MOFs comprising four-connected tetrahedral units exist in the diamond-like topology, rather than the quartz-like topology. Sun *et al.* first prepared two quartz-like, chiral, open MOFs, $Zn(ISN)_2$ (ISN = isonicotinate) with the low symmetry of α-quartz, and InH(BDC) (BDC = terephthalate) with the high symmetry of β-quartz.[14] Then Collings *et al.* experimentally found that $Zn(ISN)_2$ exhibited area-NTE in the (a,b)-plane, and InH(BDC) displayed the uniaxial-NTE along the c-axis.[25] Although there is no thermodynamic requirement that NLC and NTE must coexist, it does seem likely that a general correspondence will be observed for noncubic framework materials.[20,23] Based on this clue, large NLC behavior of InH(BDC) was found experimentally along its NTE direction by Zeng *et al.*[26] Similarly, $Zn(ISN)_2$ would be the most likely negative area compressibility (NAC) candidate by its confirmed area-NTE. On this point, it still needs experimental verification. Here, focusing on the NTE property, the physical mechanism of the area-NTE of $Zn(ISN)_2$ and uniaxial-NTE of InH(BDC) has not been studied theoretically. In diamond-like MOFs, the volume-NTE below room temperature of $Sr(C_2(COO)_2)$ had been reported.[15] Whether there will be other diamond-like MOF materials with NTE property, is still an open question. Within a specific topology, will delicate local structures and atomic linkages cause abnormal interatomic forces, that is, the elasticity anomaly? It is also worth exploring together. Based on these, in this paper, we aim to (i) uncover the underlying mechanism of area-NTE of $Zn(ISN)_2$ and uniaxial-NTE of InH(BDC), (ii) predict other diamond-like MOFs with NTE behavior, (iii) realize tunable uniaxial, area and volume NTE by changing the topology, and (iv) investigate the temperature dependence of bulk modulus in studied MOFs. It is proposed that this will be an effective way to design elaborate organic NTE materials from the simple topology in inorganic NTE materials. Moreover, it is instructive that the switching of uniaxial-NTE to area-NTE and then to volume-NTE can be achieved with fine-tuning of the geometric frame.

2. Methods and computational details

The total energy calculations are performed using the VASP code, which is based on density-functional theory (DFT). The exchange and correlation functionals are given by the generalized gradient approximation (GGA) with the Perdew–Burke–Ernzerhof (PBE) functional.[31] Electron-ion interactions are represented by the projector augmented wave (PAW) method with plane waves up to an energy of 500 eV.[32] For the sampling of the irreducible Brillouin zone, we use K-point grids of the only Gamma point for the geometry optimization. In all the calculations, self-consistency is achieved with a tolerance in the total energy of 0.1 meV. The total energy is minimized simultaneously concerning all the lattice parameters to determine the equilibrium lattice constant. The equilibrium volume is obtained by fitting the total energy as a function of volume to a three-order Murnaghan equation of state. At the fixed volume, all atoms are fully relaxed using the conjugate gradient (CG) algorithm.

The frozen-phonon approach where phonon frequencies are calculated from Hellmann–Feynman (HF) forces is employed to yield the thermodynamic properties.[33] A perturbation displacement of 0.01 Å is applied to evaluate the resulting force constants. The structures of the unit cells of studied MOFs are employed to study the lattice dynamics. Fourier interpolation is used to obtain the dynamical matrices on a $3 \times 3 \times 3$ q-point mesh. This set is used to evaluate all quantities that involve integration over phonon wave vector $\mathbf{q}$.

To study the effects of temperature, one needs to focus on free energy, incorporating the effects of thermal vibrations. The free energy of a crystal can be expressed in the quasi-harmonic approximation (QHA) as

$$F(V,T) = E(V) + F_{\text{vib}}(\omega, T)$$
$$\equiv E(V) + k_B T \sum_q \sum_j \ln\left\{ 2 \sinh\left(\frac{\hbar\omega_j(\mathbf{q})}{2k_B T} \right) \right\},$$

where E is the static contribution to the internal energy which is accessible to standard DFT calculations. $F_{\text{vib}}(\omega,T)$ represents the vibrational contribution to the free energy, and $\omega_j(\mathbf{q})$ is the frequency of the jth phonon mode at wave vector $\mathbf{q}$ in the Brillouin zone. The lattice dependence of frequency $\omega_j(\mathbf{q})$ is calculated by the frozen phonon method. Here the anharmonicity appears not only in the static internal energy $E(V)$ which includes all the anharmonic terms of the interatomic potential, but also in the lattice parameter dependence of the phonon frequency ω. The atomic motion is then approximated by a system of uncoupled normal vibrations but with different equilibrium positions and vibration frequencies. Calculations based on various semiempirical models as well as on first-principles methods demonstrate that QHA provides a reasonable description of the dynamic properties of many bulk materials below the melting point.[34,35]

$\gamma_j(\mathbf{q})$ is the mode Grüneisen parameter corresponding to the $(\mathbf{q},j)$ phonon mode, defined as

$$\gamma_j(\mathbf{q}) = -\frac{\partial \omega_j(\mathbf{q})}{\partial V} \frac{V}{\omega_j(\mathbf{q})}.$$

The $\gamma_j(\mathbf{q})$ is a primary factor for describing the contribution of a phonon mode to volumetric expansion or shrinkage. We calculate the phonon dispersion relations at different densities and approximate the derivative by the ratio of the differences to explore the contribution of the specific phonon branches. The negative values of Grüneisen parameters are unusual and mean that the frequencies $\omega_j(\mathbf{q})$ of phonon increase (or 'harden') with increasing volume, are conducive to the occurrence of abnormal physical property.

$\varepsilon[\omega_j(\mathbf{q})]$ is the mean vibrational energy of the $(\mathbf{q},j)$ phonon given by

$$\varepsilon\big[\omega_j(\mathbf{q})\big] = \hbar\omega_j(\mathbf{q})\left[\frac{1}{2} + \frac{1}{\exp\big[\hbar\omega_j(\mathbf{q})/k_{\mathrm{B}}T\big] - 1}\right].$$

Having the equation of state (EOS), we can calculate the thermal expansion and the bulk modulus as a function of temperature. The relationship between phonons and thermal expansion is established by

$$\alpha_{\mathrm{V}} = \frac{\sum \gamma_j(\mathbf{q})C_{\mathrm{V}}}{B_0}.$$

Here C_{V} is the specific heat at constant volume and B_0 is the bulk modulus. C_{V} is given by

$$C_{\mathrm{V}} = k_{\mathrm{B}}\sum_{\mathbf{q}}\sum_{j}\left(\frac{\hbar\omega_j(\mathbf{q})}{2k_{\mathrm{B}}T}\right)^2 \frac{1}{\sinh^2\big(\hbar\omega_j(\mathbf{q})/2k_{\mathrm{B}}T\big)}.$$

The temperature dependence of the B_0 is obtained from

$$B_0(T) = V\left(\frac{\partial^2 F(V,T)}{\partial V^2}\right)_T = V\frac{\partial^2 E}{\partial V^2} + V\left(\frac{\partial^2 F_{\mathrm{vib}}(\omega,T)}{\partial V^2}\right)_T.$$

3. Results and discussion

3.1. The structures of quartz-like MOFs

In hexagonal $Zn(ISN)_2$ and $InH(BDC)_2$, their frameworks are composed of a set of tetrahedral nodes Zn or In cations, linked *via* molecular ISN or BDC anions to form doubly-interpenetrated quartz nets. Despite the same topology, both have contrasting geometries. Fig. 1(a) and (b) demonstrate the main peculiarity of the crystal structures of $Zn(ISN)_2$ and $InH(BDC)_2$: the way how bonding is formed. As seen from Fig. 1(a), $Zn(ISN)_2$ with space group $P3_1$ adopts the similar characteristic of prototype α-quartz where Zn cations replace Si atoms in α-quartz, and long ISN anions replace O atoms. In contrast to the tetrahedral Zn-atom centers in $Zn(ISN)_2$, $InH(BDC)_2$ showing a highly distorted pseudo-tetrahedral geometry results in the feature structure of β-quartz (space group $P6_422$), present in Fig. 1(b). In detail, each In-atom center in $InH(BDC)_2$ connects to the other In-atom centers by linear terephthalate bridges. The resulting equilibrium lattice parameters of $Zn(ISN)_2$ and $InH(BDC)_2$ are listed in Table 1 compared with experimental data.[14] There is a good agreement between the calculated results and experimental data.

3.2. Uniaxial-NTE and area-NTE in quartz-like MOFs

As a whole, the $Zn(ISN)_2$ and $InH(BDC)_2$ show positive volume thermal expansion in the temperature range from 0 to 500 K as seen in Fig. 2(a). In our calculated results, $Zn(ISN)_2$ has a bigger

Table 1 The calculated lattice parameters of $Zn(ISN)_2$ and $InH(BDC)_2$ compared with experimental data[14]

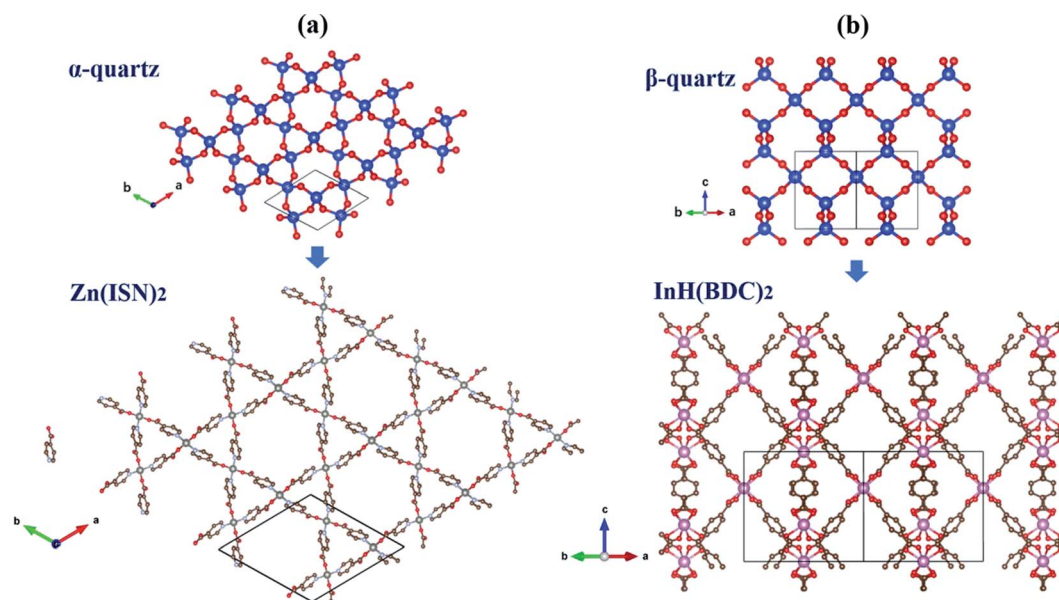|	$Zn(ISN)_2$		$InH(BDC)_2$	
	Cal.	Exp.	Cal.	Exp.
a	15.651	15.526	15.584	15.087
b	15.651	15.526	15.584	15.087
c	6.403	6.258	12.137	12.032
V	1358.21	1306.43	2553.02	2371.78

Fig. 1 (a) Crystal frameworks (supercell based on $3 \times 3 \times 1$ unit cells) of α-quartz, and $Zn(ISN)_2$ with α-quartz-like topology in a view along the *c*-axis. (b) Crystal frameworks (supercell based on $2 \times 2 \times 2$ unit cells) of β-quartz, and $InH(BDC)_2$ with β-quartz-like topology in a view along [111]. H atoms are omitted for clarity.
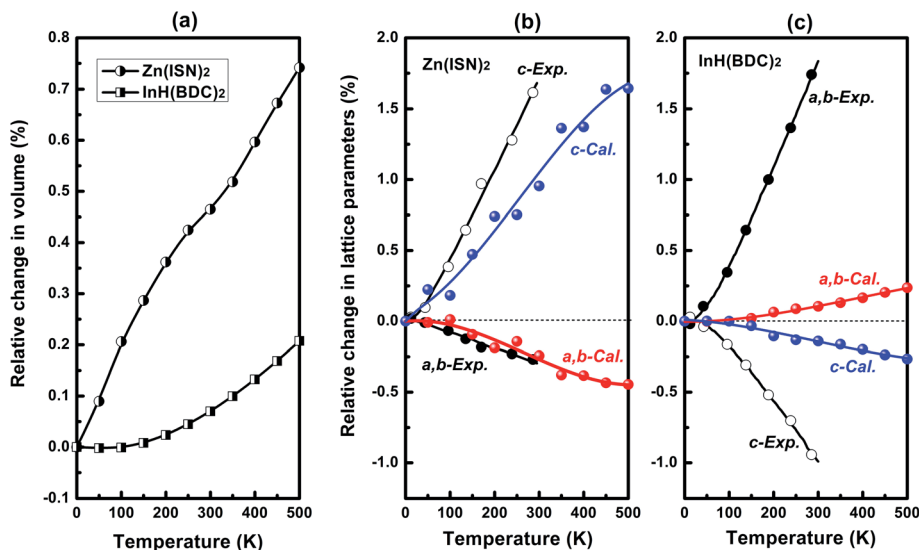
Fig. 2 (a) Calculated relative change in volume of Zn(ISN)$_2$ and InH(BDC)$_2$ as a function of temperature. Calculated relative change in lattice parameters of (b) Zn(ISN)$_2$ and (c) InH(BDC)$_2$ with increasing temperature, compared with the experimental data.[25]

relative change in volume as about three times as InH(BDC)$_2$. The relative changes in lattice parameters of Zn(ISN)$_2$ and InH(BDC)$_2$ upon heating are present in Fig. 2(b) and (c), respectively. Within the framework of QHA, our calculated values are in good agreement with the experimental data qualitatively.[25] It is particularly evident in Zn(ISN)$_2$ where the calculated area-NTE property along (a,b)-plane agrees quantitatively with the experimental data ($\alpha_{(a,b)\text{-plane}} = -21.8$ M K^{-1}). In InH(BDC)$_2$, uniaxial-NTE behavior along c-axis is confirmed by calculation (experimental value: $\alpha_c = -35$ M K^{-1}). Relative changes along different axes of InH(BDC)$_2$ in calculations are much smaller than experimental measurements, indicating InH(BDC)$_2$ has so much stronger anharmonic interaction than Zn(ISN)$_2$ that QHA can't work well. It should be noted that area-NTE is a rare phenomenon compared with uniaxial-NTE and volume-NTE. So far, only a few materials have been reported to possess this area-NTE property.[36–41] It is necessary to analyze phonon anomalies from the perspective of lattice dynamics to expand the variety of this area-NTE material and explore the contrasting responses of Zn(ISN)$_2$ and InH(BDC)$_2$ to temperature changes.

The Grüneisen parameters $\gamma_j(\mathbf{q})$ along high-symmetry directions of Zn(ISN)$_2$ and InH(BDC)$_2$ are plotted in Fig. 3. The curves of Grüneisen parameters correspond to different phonons of frequencies, the magnitudes of which are represented by the depth of color. Different from other NTE materials where acoustic phonons play an important role in NTE behavior,[5,42] it is found that low-frequency optical phonons contribute most to the area-NTE of Zn(ISN)$_2$ or uniaxial-NTE of InH(BDC)$_2$, and some high-frequency optical phonons are also associated with these abnormal properties. Fig. 3(a) and (b) have shown that compared with other ordinary phonons, low-frequency optical phonons in Zn(ISN)$_2$ and InH(BDC)$_2$ have strong negative Grüneisen parameters, while a few high-frequency phonons have slightly negative values. As far as we

know, the case, that the joint contribution from low-frequency phonons coupled with high-frequency phonons leads to NTE, is also reflected in the A$_2$M$_3$O$_{12}$ series.[43]

To analyze the vibrational modes contributing to the area-NTE of Zn(ISN)$_2$, the Eigen-displacement vectors of Zn(ISN)$_2$ corresponding to optical phonons with the strongest negative Grüneisen parameter and the second-strongest negative Grüneisen parameter at G (0, 0, 0) point are explored and displayed in Fig. 4(a) and (b), respectively. Combining these two vibrational modes, we find that Zn atoms at the hinges are stationary and the amplitudes of O atoms are small, but those of C and N atoms are very strong. It is worth noting that pyridines composed of C and N atoms involve rotational vibration. Although the directions of the rotational vibrations are different in the two phonon modes, both can cause the wrinkles of the covalent chains of Zn–pyridine–Zn linkages and then lead to the shortening of the a-axis and b-axis in Zn(ISN)$_2$ upon heated, *i.e.* the area-NTE of Zn(ISN)$_2$. Moreover, the rotational vibrations of some pyridines are not along the directions of the chains of Zn–pyridine–Zn linkages but will be deflected, leading to the decreased angle θ between the a-axis and b-axis. The diagrammatic sketch of structural deformation caused by rotational vibration of pyridine is shown in Fig. 4(c).

Concerning the origin of uniaxial-NTE of InH(BDC)$_2$, some specific Eigen-displacement vectors of phonon modes are analyzed. Fig. 5(a) presents the vibrational modes of InH(BDC)$_2$ with the strongest negative Grüneisen parameter at G (0, 0, 0) point. It is noticed that the In atoms are stationary and the amplitudes of C atoms are very small. That means that the benzene ring has little contribution to the whole. However, the O atoms connected to In atoms have a very strong amplitude, so the vibrations of the O atoms become the key to the characteristics of this phonon mode. We extract this In–O local structure as a detailed analysis object shown in Fig. 5(b). Eight O atoms connected to one In atom have symmetrical directions
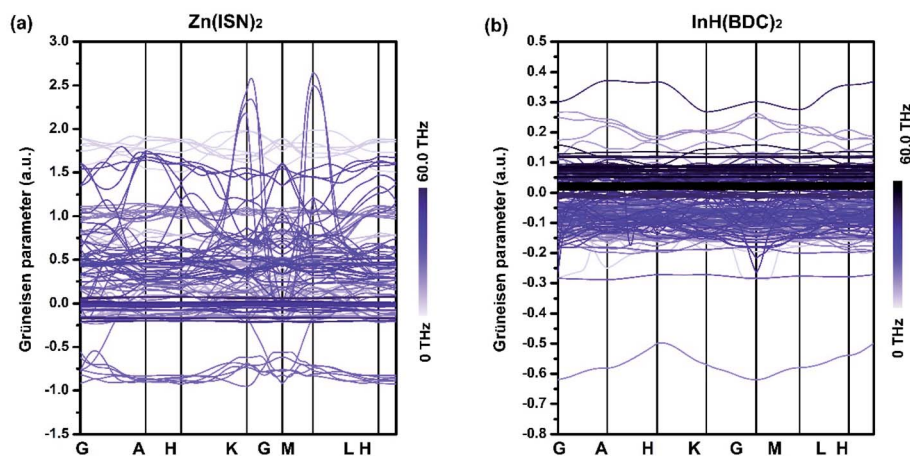
Fig. 3 (a) Calculated mode Grüneisen parameters along high-symmetry directions in Brillouin zone of (a) $Zn(ISN)_2$ and (b) $InH(BDC)_2$. The curves of mode Grüneisen parameters correspond to phonon modes of different frequencies which are represented by the depth of the color.

of vibration. Such vibration vectors result in the transverse component forces that are opposite to each other in the (a,b)-plane, thus reducing the angle θ between the chains of In–O–Benzene–In linkages and (a,b)-plane. In this case, the c-axis of $InH(BDC)_2$ is shortened. This vibrational mode plays a decisive role in the uniaxial-NTE of $InH(BDC)_2$, and the corresponding structural deformation diagram is shown in Fig. 5(c). Another characteristic vibrational mode of $InH(BDC)_2$ with the second-strongest negative Grüneisen parameter at G (0, 0, 0) point is exhibited in Fig. 5(d). It is seen that In atoms at the hinges act and have strong amplitudes, while the amplitudes of O atoms are not strong and have the opposite vibrational directions to In atoms. The C atoms have various amplitudes and vibrational directions, which makes the benzene ring have distorted

vibration and the chains of In–O–Benzene–In linkages will be slightly bent. The local structure of the In–O–Benzene ring is stripped from the crystal and shown in Fig. 5(e). The opposite vibration direction of In atoms and other nonmetal atoms shortens the distance between the chains of In–O–Benzene–In linkages and (a,b)-plane, which leads to the contraction of the c-axis. The corresponding deformation schematic of crystal structure in $InH(BDC)_2$ is displayed in Fig. 5(f), where the slight deformation of the benzene ring is considered as quasi-rigid here.[43]

3.3. Bulk modulus anomaly in α-quartz-like MOFs

Adequate knowledge of the temperature dependence of the bulk modulus is necessary for understanding the thermoelastic and
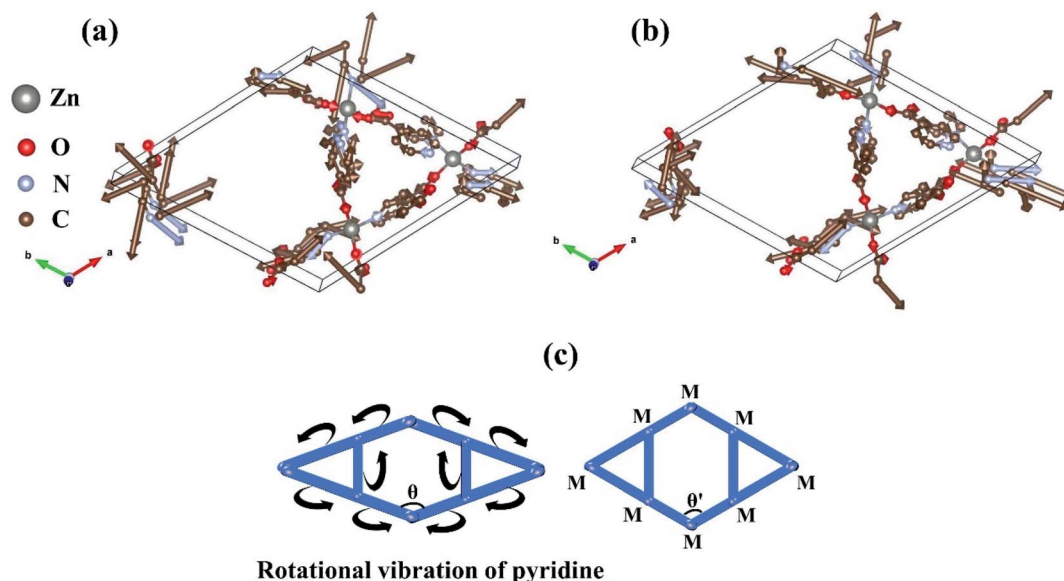

Fig. 4 Eigen-displacement vectors of phonon modes with (a) the strongest negative Grüneisen parameter and (b) the second-strongest negative Grüneisen parameter at G (0, 0, 0) point, that are involved in the area-NTE of $Zn(ISN)_2$. Arrows are proportional to the amplitude of the atomic motion. (c) Structural deformation diagram in which rotational vibration of pyridine as extracted feature of vibration mode according to the vector analysis of (a) and (b). M represents the metal (Zn) atom. H atoms are deleted since their vibrations are not considered here.
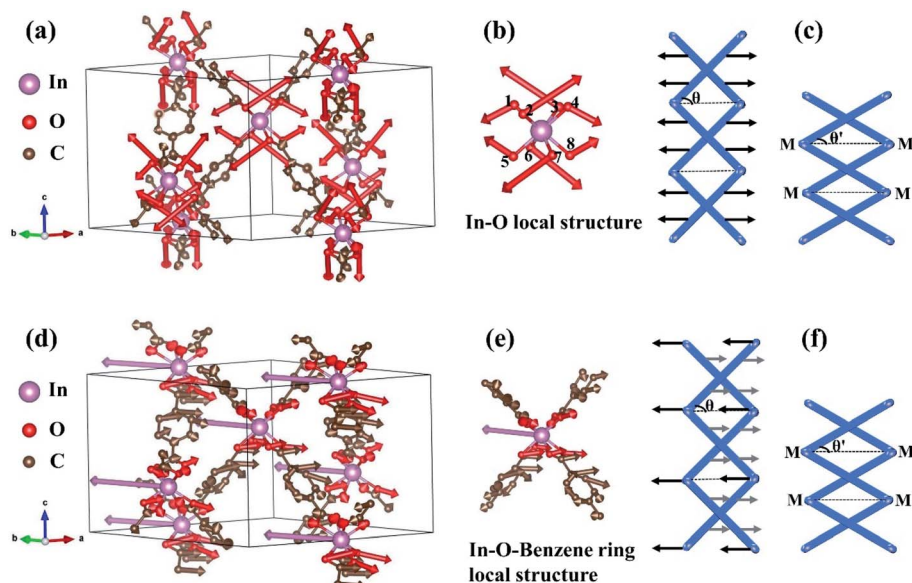
Fig. 5 (a) Eigen-displacement vectors of phonon modes in InH(BDC)$_2$ with the strongest negative Grüneisen parameter at G (0, 0, 0) point. The corresponding vibrational modes of In–O local structure and schematic representations of the deformations of crystal structure in InH(BDC)$_2$ are present in (b) and (c), respectively. (d) Eigen-displacement vectors of phonon modes in InH(BDC)$_2$ with the second-strongest negative Grüneisen parameter at G (0, 0, 0) point. (e) and (f) show the corresponding vibrational modes of In–O–Benzene ring local structure, and schematic of the deformations of crystal structure in InH(BDC)$_2$, respectively. M represents the metal (In) atom. H atoms are deleted since their vibrations are not considered here.

anharmonic properties of crystals. Elasticity provides more information than the volume in understanding temperature dependence of the equation of state (EOS) because the compressibility or bulk modulus is defined by the derivative of the volume. Thus, the bulk modulus is more sensitive to the variation in EOS than volume. The temperature dependence of bulk modulus of Zn(ISN)$_2$ and InH(BDC)$_2$ are calculated and shown in Fig. 6(a) and (b), respectively. At 0 K, the bulk modulus of Zn(ISN)$_2$ is about 60 GPa as much as five times that of

InH(BDC)$_2$, showing Zn(ISN)$_2$ has a natural stronger interatomic force than InH(BDC)$_2$. Normally, the changing trend of bulk modulus in the external field (temperature or pressure) is inversely dependent on that of volume. It follows that the bulk modulus decreases (increases) with the increase of temperature in PTE materials (volume-NTE materials). For instance, a typical isotropic MOF-5 compound with volume-NTE exhibits that the bulk modulus increases upon heating.[44] Concerning Zn(ISN)$_2$ and InH(BDC)$_2$, they show a completely different trend of bulk modulus with the increase of temperature. It is noted that the bulk modulus anomaly occurs in Zn(ISN)$_2$ where the changing trend of the bulk modulus is consistent abnormally with that of volume when heated.

From theoretical considerations, an equation is derived by Anderson in the fundamental constant of a solid:[45]

$$\frac{\mathrm{d}B_0}{\mathrm{d}T} = -\delta_T \gamma \frac{C_V}{V}.$$

The isothermal Anderson–Grüneisen parameter δ_T, a parameter to estimate the abnormal temperature dependence of bulk modulus, is defined as:

$$\delta_T = -\frac{1}{\alpha B_0} \left(\frac{\mathrm{d}B_0}{\mathrm{d}T} \right)_P,$$

where α is the coefficient of volume thermal expansion, the B_0 is the bulk modulus.

The Anderson–Grüneisen parameter δ_T, similar in many respects to the Grüneisen parameter γ, yields important information about the interatomic forces and enables us to predict the macroscopic behavior of different thermal properties for
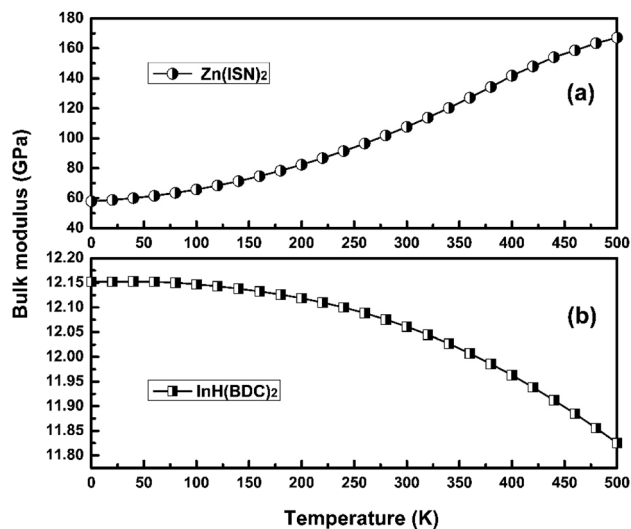

Fig. 6 The temperature dependence of bulk modulus of (a) Zn(ISN)$_2$ and (b) InH(BDC)$_2$.

which, at present, experimental data or theory alone is inadequate. Commonly, δ_T is positive, indicating a normal temperature dependence of bulk modulus. If δ_T is negative, it will show the abnormal relationship between bulk modulus and temperature. The negative δ_T of $Zn(ISN)_2$ and the positive δ_T of $InH(BDC)_2$ can be obtained by the simple symbolic estimation of the formula. The interatomic forces in $Zn(ISN)_2$ with α-quartz-like topology are gradually increasing, indicating $Zn(ISN)_2$ is not easily compressional when heated. Here, it can be predicted that the bulk modulus anomaly is more likely to occur in some other MOFs with α-quartz-like topology.

3.4. Volume-NTE in diamond-like MOFs

Another typical structural motif of MOFs is the diamond-like topology, by which MOFs access a variety of geometries. A series of MOFs with diamond-like topology are selected and calculated to explore possible anomalous NTE properties. Finally, we lock in four MOFs with volume-NTE behavior, which are $Ag(4\text{-}cnpy)_2$ (space group: $Pbca$), $Co(5\text{-}X\text{-}2\text{-}pymo)_2$ (space group: $I\bar{4}2d$), $Cu(2,5\text{-}Me_2pyz)_2$ (space group: $P2_1/n$), and $Zn(PT)_2$ (space group: $P2_1/n$).[27–30] The crystal frameworks of these four MOFs are shown in Fig. 7(a)–(d), respectively. Although these MOFs with diamond-like topology have volume-NTE behavior, their temperature ranges of volume-NTE are quite different. It is exhibited in Fig. 8 that the volume-NTE of $Ag(4\text{-}cnpy)_2$ and $Co(5\text{-}X\text{-}2\text{-}pymo)_2$ can be extended to 1000 K, while that of $Cu(2,5\text{-}Me_2pyz)_2$ and $Zn(PT)_2$ only exist in the region of 0–500 K. Moreover, the volume-NTE of $Ag(4\text{-}cnpy)_2$ and $Co(5\text{-}X\text{-}2\text{-}pymo)_2$ is much stronger than that of $Cu(2,5\text{-}Me_2pyz)_2$ and $Zn(PT)_2$. Previous literature has speculated that these materials are potential area-NTE/NAC or uniaxial-NTE/NLC materials,[25] but through our study of their axial behavior, we find that these materials only show volume anomalies, not axial anomalies. This still needs further experimental verification.

So far, various abnormal behaviors from uniaxial-NTE, area-NTE to volume-NTE in MOFs have been achieved based on quartz-like and diamond-like topologies. Moreover, in the preparation of MOFs with these specific topologies, the flexibility of the framework can be further adjusted by changing the length of the internal organic chain, thus realizing the regulation of the size of various NTE behaviors.[5]

3.5. Bulk-modulus anomaly in diamond-like MOFs

The temperature dependence of bulk modulus in these MOFs with the diamond-like framework is also studied. It is found that the bulk modulus anomaly will still appear. In Fig. 9(a), the bulk modulus of $Ag(4\text{-}cnpy)_2$ will increase with increased temperature. This is normal elastic behavior, that is, the changing trend of the bulk modulus is inversely dependent on that of volume. The volume of $Ag(4\text{-}cnpy)_2$ decreases with the increase of temperature, and then the interatomic force increases, and the bulk modulus finally shows an increasing trend. Above 500 K, the PTE behavior of $Cu(2,5\text{-}Me_2pyz)_2$ begins to appear as seen in Fig. 8(b), but its bulk modulus has no inflection point and continues to increase with the increase of temperature in Fig. 9(b), showing the abnormal bulk modulus in the high-temperature region. About $Zn(PT)_2$ and $Co(5\text{-}X\text{-}2\text{-}pymo)_2$, both of them exhibit bulk-modulus anomaly within the temperature range studied in Fig. 9(c) and (d), where the bulk modulus – temperature relationship is consistent anomalously with the volume – temperature relationship. In other NTE materials, abnormal elastic properties are rare, but in MOFs, it seems that elastic properties anomaly and abnormal NTE behaviors are more likely to be accompanied. These specific topologies (quartz-like, diamond-like, and so on) provide an
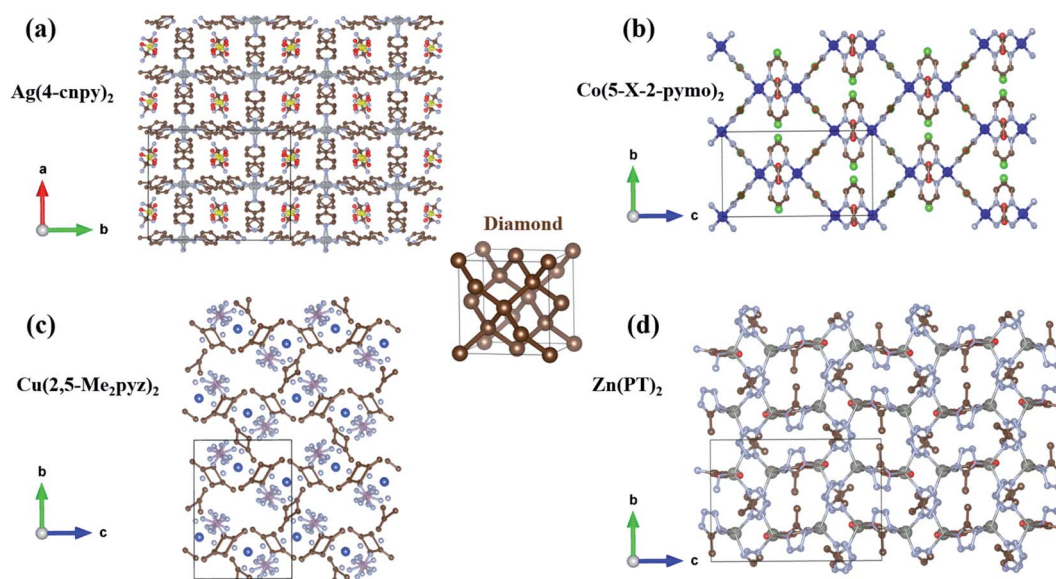

Fig. 7 The crystal framework structures (supercell based on 2 × 2 × 2 unit cells) of diamond-like MOFs of (a) $Ag(4\text{-}cnpy)_2$, (b) $Co(5\text{-}X\text{-}2\text{-}pymo)_2$, (c) $Cu(2,5\text{-}Me_2pyz)_2$, and (d) $Zn(PT)_2$. H atoms are omitted for clarity. Abbreviations used: 4-cnpy = 4-cyanopyridine, 5-X-2-pymo = 5-halopyrimidin-2-ol (X = Be/I), 2,5-Me_2pyz = 2,5-dimethylpyrazine, PT = 5-propyltetrazole.
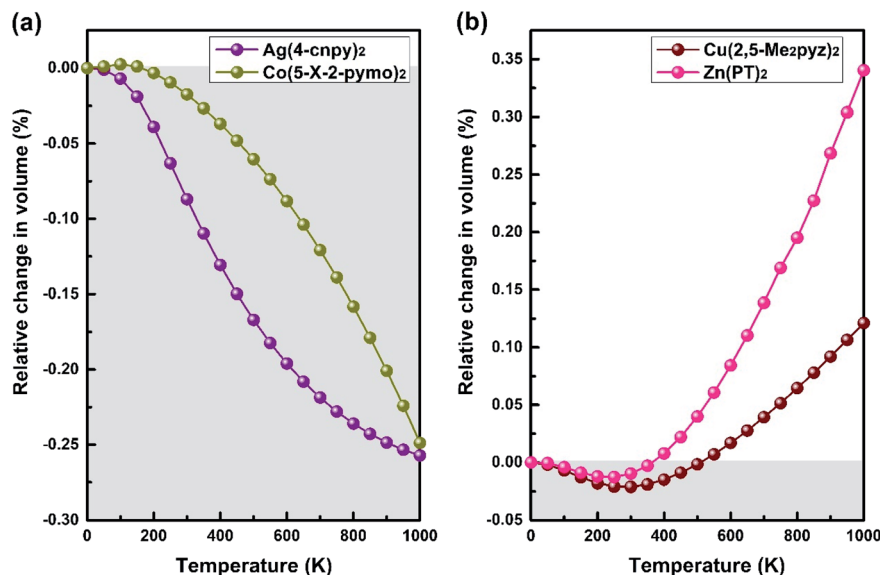
Fig. 8 (a) Calculated relative change in volume of Ag(4-cnpy)$_2$ and Co(5-X-2-pymo)$_2$, which exhibit the volume-NTE up to 1000 K. (b) Calculated relative change in volume of Cu(2,5-Me$_2$pyz)$_2$ and Zn(PT)$_2$, whose volume-NTE behaviors exist in the region of 0–500 K.
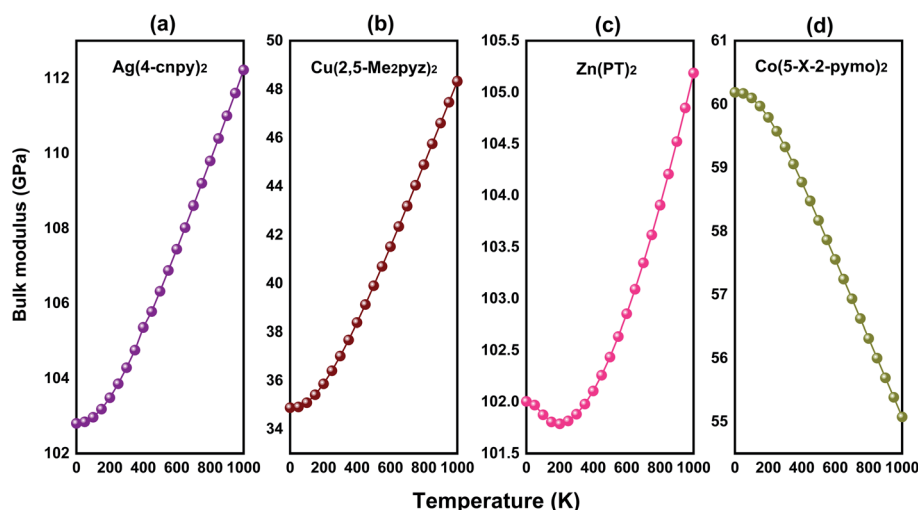
Fig. 9 The temperature dependence of bulk modulus of (a) Ag(4-cnpy)$_2$, (b) Cu(2,5-Me$_2$pyz)$_2$, (c) Zn(PT)$_2$, and (d) Co(5-X-2-pymo)$_2$.

important geometric framework for various NTE behaviors of MOFs, but at the same time, the local structure and bond environment in MOFs may lead to other abnormal properties, such as bulk-modulus anomaly. If the bond linkage is close to linear, it will cause the normal changing trend of interatomic force in the external field. If there is an angle between the links of these bonds, the changing trend of abnormal interatomic forces will probably appear, namely, a variety of abnormal elastic properties are possible. Here, we also hope that this elastic property of MOFs can attract more attention and exploration.

4. Conclusion

In conclusion, various NTE behaviors from the uniaxial, area, and volume-NTE can be realized in MOFs with quartz-like and

diamond-like frameworks. The area-NTE of Zn(ISN)$_2$ and uniaxial-NTE of InH(BDC) have been studied. Their thermal behaviors in calculations agree well with the experimental data. According to the calculation of Grüneisen parameters, low-frequency optical phonons contribute most to area-NTE of Zn(ISN)$_2$ and uniaxial-NTE of InH(BDC). It is worth noting that some high-frequency phonons also play a role. The vibrational eigenvectors of some key phonons are analyzed in detail. The rotational vibration of pyridine in Zn(ISN)$_2$, and transverse vibration of In–O local structure and In–O–Benzene ring local structure in InH(BDC) are identified. Furthermore, four MOFs with the diamond-like framework are predicted to possess volume-NTE behavior. It still needs to be verified by experiments. In some studied MOFs, the abnormal bulk modulus with increasing temperature is found. Although these specific

topologies provide an important geometric framework for various NTE behaviors of MOFs, the local structure and bond environment may be associated with the abnormal interatomic force, leading to the bulk modulus anomaly.

Conflicts of interest

There are no conflicts to declare.

Acknowledgements

References

1 M. T. Dove and H. Fang, Negative thermal expansion and associated anomalous physical properties: review of the lattice dynamics theoretical foundation, *Rep. Prog. Phys.*, 2016, **79**, 066503.

2 C. Wang, L. Chu, Q. Yao, Y. Sun, M. Wu, L. Ding, J. Yan, Y. Na, W. Tang and G. Li, Tuning the range, magnitude, and sign of the thermal expansion in intermetallic $Mn_3(Zn, M)_xN$ (M=Ag, Ge), *Phys. Rev. B: Condens. Matter Mater. Phys.*, 2012, **85**, 220103.

3 J. Chen, X. Xing, C. Sun, P. Hu, R. Yu, X. Wang and L. Li, Zero thermal expansion in $PbTiO_3$-based perovskites, *J. Am. Chem. Soc.*, 2008, **130**, 1144–1145.

4 K. Takenaka, Negative thermal expansion materials: technological key for control of thermal expansion, *Sci. Technol. Adv. Mater.*, 2012, **13**, 013001.

5 L. Wang, M. T. Dove, J. Shi, B. Sun, D. Hu and C. Wang, Adjustable uniaxial zero thermal expansion and zero linear compressibility in unique hybrid semiconductors: the role of the organic chain, *Dalton Trans.*, 2020, **49**, 719–728.

6 L. Wang and C. Wang, Negative/zero thermal expansion in black phosphorus nanotubes, *Phys. Chem. Chem. Phys.*, 2018, **20**, 28726–28731.

7 G. Barrera, J. Bruno, T. Barron and N. Allan, Negative thermal expansion, *J. Phys.: Condens. Matter*, 2005, **17**, R217–R252.

8 K. Wang, M. Feng, L. Zhou, J. Li, X. Qi and X. Huang, A hybrid with uniaxial negative thermal expansion behaviour: the synergistic role of organic and inorganic components, *Chem. Commun.*, 2014, **50**, 14960–14963.

9 J. Li, W. Bi, W. Ki, X. Huang and S. Reddy, Nanostructured crystals: unique hybrid semiconductors exhibiting nearly zero and tunable uniaxial thermal expansion behavior, *J. Am. Chem. Soc.*, 2007, **129**, 14140–14141.

10 G. Artioli, M. Dapiaggi, P. Fornasini, A. Sanson, F. Rocca and M. Merli, Negative thermal expansion in cuprite-type compounds: a combined synchrotron XRPD, EXAFS, and computational study of Cu_2O and Ag_2O, *J. Phys. Chem. Solids*, 2006, **67**, 1918–1922.

11 T. Chatterji, M. Zbiri and T. C. Hansen, Negative thermal expansion in ZnF_2, *Appl. Phys. Lett.*, 2011, **98**, 181911.

12 L. Wang, P. Yuan, F. Wang, Q. Sun, Z. Guo, E. Liang and Y. Jia, First-principles investigation of negative thermal expansion in II-VI semiconductors, *Mater. Chem. Phys.*, 2014, **148**, 214–222.

13 P. Deus and H. Schneider, Thermal expansion of the diamond-like semiconducting compound $ZnSiP_2$ within the temperature range 20 to 300 K, *Phys. Status Solidi A*, 1983, **79**, 411–415.

14 J. Sun, L. Weng, Y. Zhou, J. Chen, Z. Chen, Z. Liu and D. Zhao, QMOF-1 and QMOF-2: three-dimensional metal–organic open frameworks with a quartzlike topology, *Angew. Chem., Int. Ed.*, 2002, **41**, 4471–4473.

15 F. Hohn, I. Pantenburg and U. Ruschewitz, $Sr[C_2(COO)_2]$: the first anhydrous salt of acetylenedicarboxylic acid, *Chem.– Eur. J.*, 2002, **8**, 4536–4541.

16 G. A. Lager, J. Jorgensen and F. Rotella, Crystal structure and thermal expansion of α-quartz SiO_2 at low temperatures, *J. Appl. Phys.*, 1982, **53**, 6751–6756.

17 P. Welche, V. Heine and M. Dove, Negative thermal expansion in beta-quartz, *Phys. Chem. Miner.*, 1998, **26**, 63–77.

18 A. L. Goodwin, M. Calleja, M. J. Conterio, M. T. Dove, J. S. O. Evans, D. A. Keen, L. Peters and M. G. Tucker, Colossal positive and negative thermal expansion in the framework material $Ag_3[Co(CN)_6]$, *Science*, 2008, **319**, 794–797.

19 A. L. Goodwin, D. A. Keen and M. G. Tucker, Large negative linear compressibility of $Ag_3[Co(CN)_6]$, *Proc. Natl. Acad. Sci. U. S. A.*, 2008, **105**, 18708–18713.

20 L. Wang, C. Wang, H. Luo and Y. Sun, The correlation between uniaxial negative thermal expansion and negative linear compressibility in $Ag_3[Co(CN)_6]$, *J. Phys. Chem. C*, 2017, **121**, 333–341.

21 A. L. Goodwin, B. J. Kennedy and C. J. Kepert, Thermal expansion matching via framework flexibility in zinc dicyanometallates, *J. Am. Chem. Soc.*, 2009, **131**, 6334–6335.

22 A. B. Cairns, J. Catafesta, C. Levelut, J. Rouquette, A. Van Der Lee, L. Peters, A. L. Thompson, V. Dmitriev, J. Haines and A. L. Goodwin, Giant negative linear compressibility in zinc dicyanoaurate, *Nat. Mater.*, 2013, **12**, 212–216.

23 L. Wang, H. Luo, S. Deng, Y. Sun and C. Wang, Uniaxial negative thermal expansion, negative linear compressibility, and negative Poisson's ratio induced by specific topology in $Zn[Au(CN)_2]_2$, *Inorg. Chem.*, 2017, **56**, 15101–15109.

24 S. L. James, Metal-organic frameworks, *Chem. Soc. Rev.*, 2003, **32**, 276–288.

25 I. E. Collings, M. G. Tucker, D. A. Keen and A. L. Goodwin, Geometric switching of linear to area negative thermal expansion in uniaxial metal–organic frameworks, *CrystEngComm*, 2014, **16**, 3498–3506.

© 2022 The Author(s). Published by the Royal Society of Chemistry

26 Q. Zeng, K. Wang and B. Zou, Large negative linear compressibility in InH(BDC)₂ from framework hinging, *J. Am. Chem. Soc.*, 2017, **139**, 15648–15651.

27 L. Carlucci, G. Ciani, D. M. Proserpio and A. Sironi, Interpenetrating diamondoid frameworks of silver (I) cations linked by N,N′-bidentate molecular rods, *J. Chem. Soc., Chem. Commun.*, 1994, **24**, 2755–2756.

28 T. Otieno, S. J. Rettig, R. C. Thompson and J. Trotter, Complex polymeric cations of copper (I) with graphite-and diamond-related lattices; crystal structures of poly-tris (. mu.-2, 5-dimethylpyrazine) dicopper (I) hexafluorophosphate and poly-bis (. mu.-2, 5-dimethylpyrazine) copper (I) hexafluorophosphate, *Inorg. Chem.*, 1993, **32**, 1607–1611.

29 L. Ma, Y. C. Qiu, G. Peng, J. B. Cai and H. Deng, In situ tetrazole ligand synthesis of two-fold interpenetrating zinc coordination frameworks, *Eur. J. Inorg. Chem.*, 2011, **23**, 3446–3453.

30 N. Masciocchi, S. Galli, A. Sironi, E. Cariati, M. A. Galindo, E. Barea, M. A. Romero, J. M. Salas, J. A. Navarro and F. Santoyo-González, Tuning the structural and magnetic properties of thermally robust coordination polymers, *Inorg. Chem.*, 2006, **45**, 7612–7620.

31 J. P. Perdew, K. Burke and M. Ernzerhof, Generalized gradient approximation made simple, *Phys. Rev. Lett.*, 1996, **77**, 3865.

32 G. Kresse and J. Furthmüller, Efficient iterative schemes for ab initio total-energy calculations using a plane-wave basis set, *Phys. Rev. B: Condens. Matter Mater. Phys.*, 1996, **54**, 11169.

33 A. Togo, F. Oba and I. Tanaka, First-principles calculations of the ferroelastic transition between rutile-type and CaCl₂-type SiO₂ at high pressures, *Phys. Rev. B: Condens. Matter Mater. Phys.*, 2008, **78**, 134106.

34 L. Wang, C. Wang, Y. Sun, S. Deng, K. Shi, H. Lu, P. Hu and X. Zhang, First-principles study of Sc₁₋ₓTiₓF₃ (x ≤ 0.375): negative thermal expansion, phase transition, and compressibility, *J. Am. Ceram. Soc.*, 2015, **98**, 2852–2857.

35 L. Wang, P. Yuan, F. Wang, Q. Sun, E. Liang, Y. Jia and Z. Guo, Negative thermal expansion in TiF₃ from the first-principles prediction, *Phys. Lett. A*, 2014, **378**, 2906–2909.

36 I. Grobler, V. J. Smith, P. M. Bhatt, S. A. Herbert and L. J. Barbour, Tunable anisotropic thermal expansion of a porous zinc (II) metal–organic framework, *J. Am. Chem. Soc.*, 2013, **135**, 6411–6414.

37 D. Das, T. Jacobs and L. J. Barbour, Exceptionally large positive and negative anisotropic thermal expansion of an organic crystalline material, *Nat. Mater.*, 2010, **9**, 36–39.

38 M. J. Cliffe and A. L. Goodwin, PASCal: a principal axis strain calculator for thermal expansion and compressibility determination, *J. Appl. Crystallogr.*, 2012, **45**, 1321–1329.

39 S. J. Hibble, A. M. Chippindale, A. H. Pohl and A. C. Hannon, Surprises from a simple material-the structure and properties of nickel cyanide, *Angew. Chem., Int. Ed.*, 2007, **119**, 7246–7248.

40 S. A. Hodgson, J. Adamson, S. J. Hunt, M. J. Cliffe, A. B. Cairns, A. L. Thompson, M. G. Tucker, N. P. Funnell and A. L. Goodwin, Negative area compressibility in silver (I) tricyanomethanide, *Chem. Commun.*, 2014, **50**, 5264–5266.

41 M. Y. Seyidov and R. A. Suleymanov, Negative thermal expansion due to negative area compressibility in TlGaSe₂ semiconductor with layered crystalline structure, *J. Appl. Phys.*, 2010, **108**, 063540.

42 L. Wang, C. Wang and Y. Chen, Black phosphorene exhibiting negative thermal expansion and negative linear compressibility, *J. Phys.: Condens. Matter*, 2019, **31**, 465003.

43 L. Wang, F. Wang, P. Yuan, Q. Sun, E. Liang, Y. Jia and Z. Guo, Negative thermal expansion correlated with polyhedral movements and distortions in orthorhombic Y₂Mo₃O₁₂, *Mater. Res. Bull.*, 2013, **48**, 2724–2729.

44 L. Wang, C. Wang, Y. Sun, K. Shi, S. Deng and H. Lu, Large negative thermal expansion provided by metal-organic framework MOF-5: a first-principles study, *Mater. Chem. Phys.*, 2016, **175**, 138–145.

45 M. Madan, Temperature dependence of the bulk modulus of alkali halides, *J. Appl. Phys.*, 1971, **42**, 3888–3893.